A Study of the Impacts of Vertical Diffusion on the Structure and Intensity of the Tropical Cyclones Using the High Resolution HWRF system

Sundararaman G. Gopalakrishnan[1], Frank Marks, Jr[1], Jun A. Zhang[2], Xuejin Zhang[2], Jian-Wen Bao[3] and Vijay Tallapragada[4]

[1] NOAA/ Atlantic Oceanographic and Meteorological Laboratory/ Hurricane Research Division, Miami, FL, USA;

[2] University of Miami, Cooperative Institute for Marine and Atmospheric Studies, Miami, FL, USA;

[3] NOAA/Earth System Research Laboratory Boulder, CO, USA;

[4] NOAA/Environmental Modeling Center, National Centers for Environmental Predictions, Washington, DC, USA

(Revised version submitted to the Journal of the Atmospheric Sciences: July 31, 2012)

Corresponding author address: S.G. Gopalakrishnan, AOML/HRD, 4301 Rickenbacker Causeway, Miami, Florida 33149

<E-mail: gopal@noaa.gov>

Abstract

The Hurricane Weather Research and Forecasting (HWRF) system was used in an idealized framework to gain a fundamental understanding of the variability in TC structure and intensity prediction that may arise due to vertical diffusion. The modeling system uses the Medium-Range Forecast parameterization scheme. Flight-level data collected by a NOAA WP-3D research aircraft during the eyewall penetration of category 5 Hurricane Hugo (1989) at an altitude of about 450-500 m and Hurricane Allen (1980) were used as the basis to best match the modeled eddy diffusivities with wind speed. While reduction of the eddy diffusivity to a quarter of its original value produced the best match with the observations, such a reduction revealed a significant decrease in the height of the inflow layer as well which, in turn, drastically impacted the size and intensity changes in the modeled TC. The cross-isobaric flow (inflow) was observed to be stronger with the decrease in the inflow depth. Stronger inflow not only increased the spin of the storm, enhancing the generalized Coriolis term in the equations of motion for tangential velocity, but also resulted in enhanced equivalent potential temperature in the boundary layer, a stronger and warmer core and, subsequently, a stronger storm. More importantly, rapid acceleration of the inflow not only produced a stronger outflow at the top of the inflow layer, more consistent with observations, but also a smaller inner core that was less than half the size of the original.

1. Introduction

The upward transfer of moisture and heat from the ocean surface to the atmosphere and the downward transfer of momentum from the atmosphere to the ocean surface by turbulence mixing processes within the hurricane boundary layer[1] have long been known to play an important role in regulating the radial and vertical distribution of enthalpy and momentum and, consequently, intensity changes in hurricanes (e.g., Malkus and Riehl 1960; Rosenthal 1962; Smith 1968; Ooyama 1969; Kurihara and Tuleya 1974; Anthes and Chang 1978; Tuleya and Kurihara 1978; Emanuel 1986, 1995). In fact, as early as in the 1960s, Smith (1968) used a simple analytical model to examine some of the features of the hurricane boundary layer by varying the eddy diffusivities. He concluded, however, that inadequate knowledge of the turbulence structure at that time prevented a more realistic understanding of the layer. To date, even with the best forecast models for tropical cyclone (TC) prediction operating at the highest resolution it is still not possible to resolve these transport and diffusive processes in the lower atmosphere. Hence, subgrid scale parameterization schemes are required. These parameterization schemes are usually dependent on four key parameters, namely, surface exchange coefficients for momentum (Cd), moisture and heat (Ck), eddy diffusivity for momentum (Km), and moisture and heat (Kh). These parameters determine the transfer and diffusion of fluxes from the atmosphere to the underlying ocean surface and vice-versa. However, there is a large degree of uncertainty in the estimates of these parameters. Consequently, the structure and intensification of TCs as simulated by high-resolution mesoscale models are sensitive to the surface and planetary boundary layer

[1] Depth of the inflow layer is generally adopted to be the height of the hurricane boundary layer. However, significant turbulence and mixing may occur above this layer, especially in the eyewall region

(PBL) parameterizations used in these models (e.g., Braun and Tao 2000; Nolan et al. 2009a,b; Montgomery et al. 2010; Smith and Thomsen 2010). Nevertheless, based on observations (Powell et al. 2003), laboratory experiments (Donelan et al. 2004), and some modeling work (Moon et al. 2004 a, b), a better understanding of Cd, especially in the high wind regime, has been attained in recent times. A synthesis of observations from the Coupled Boundary Layer Air-Sea Transfer Experiment (CBLAST) (Black et al. 2007; Zhang 2007; Zhang et al. 2008) has also provided evidence on the observed behavior of Ck in moderate wind regions, especially between 15-30 m s^{-1}. Recent laboratory experiments (Haus et al. 2010) and the theoretical study of Montgomery et al. (2010) present additional evidence to confirm a constant behavior of Ck above wind speeds of about 30 m s^{-1}. A value of about 1.2-1.3 x 10^{-3} for Ck appears to be a reasonable estimate. However, very little is known about mixing (Km and Kh) above the surface layer.

Flight-level data collected by a NOAA WP-3D research aircraft during the eyewall penetration of category 5 Hurricane Hugo (1989) at an altitude of about 450-500 m (Marks et al. 2008) and Hurricane Allen (1980) (Marks 1985) provide a unique opportunity for estimating eddy diffusivities. These estimates are important for evaluating numerical models. Based on an analysis of the flight-level data for these two intense storms, Zhang et al. (2011a) provided estimates of the eddy diffusivity coefficient in the hurricane boundary layer with the maximum Km (and Kh) values varying between 38-101 m^2 s^{-1}. These estimates are consistent with estimates from the theoretical and numerical studies of Kepert (2001) and Smith (2003). More recently, Zhang et al. (2011b) used data from 794 GPS dropsondes deployed by NOAA research aircraft in 13 hurricanes to study the characteristic height scale of the hurricane PBL. A composite

analysis from their study demonstrates that the height of the inflow layer increases with increasing radius from the center of strong storms (categories 4-5 on the Saffir-Simpson scale), with a minimum inflow layer depth of about 900 m near the eye to about 1200 m at a distance of about five times the radius of the maximum wind. These data sets are used to evaluate the PBL parameterization in the Hurricane Weather Research and Forecast (HWRF) system described here.

A simple first-order vertical diffusion parameterization scheme based on the local Richardson number for determining Km and Kh has been in use in NCEP's Medium-Range Forecast (MRF) model since the 1980s, and an upgraded version based on the non-local K approach valid within the well-mixed boundary layer (Hong and Pan 1996) has been used in the Global Forecasting System (GFS) since the 1990s. The "so called" GFS scheme is also used in a suite of operational models such as the Geophysical Fluid Dynamics Laboratory's (GFDL) hurricane model and the HWRF system, among others. The GFS scheme has also been an option in research models such as the fifth-generation NCAR/Pennsylvania State University mesoscale model (MM5). Braun and Tao (2000) studied the sensitivity of high-resolution simulations of Hurricane Bob (1991) to PBL parameterizations. This study used four PBL parameterization schemes (namely, a simple bulk aerodynamic scheme, a local Richardson number and mixing length based Blackadar scheme, the GFS, and a high-order, Turbulence Kinetic Energy based Burk–Thompson boundary layer scheme) and compared their eyewall structure, storm intensity, and boundary layers, illustrating the sensitivity of surface exchange and subsequent vertical mixing processes on TC structure and intensity predictions. The study also found that the GFS scheme in MM5 produced weaker and deeper inflow and that the strong

outflow at the top of the inflow layer was absent when compared to the other schemes. Additionally, the GFS scheme produced the weakest storm.

Recently, several studies (e.g., Nolan et al. 2009a,b; Smith and Thomsen, 2010 and Bao et al. 2011) have illustrated the sensitivity of modeled surface and PBL schemes to hurricane structure and intensity predictions. For instance, Nolan et al. (2009a,b) provided an extensive evaluation of PBL parameterizations in TCs by comparing in situ observations to high-resolution simulations of Hurricane Isabel (2003). In particular, the authors used the Yonsei University (YSU) parameterization and the Mellor–Yamada–Janjic (MYJ) parameterization available within the Weather Research and Forecasting (WRF) modeling framework. They found that by modifying the original YSU and MYJ schemes to ocean roughness lengths more in agreement with previous observations (Donelan et al. 2004), improved predictions were possible for the simulation of Hurricane Isabel, as measured by standard metrics of track and 10-m winds. When compared with CBLAST observations obtained during Hurricane Isabel, both schemes reproduced the structure remarkably well. Nevertheless, the authors did notice differences in the structure modeled by the two schemes. Smith and Thomsen (2010) demonstrated a dependence of TC intensification on the boundary-layer representation in MM5. Predictions using one of five available schemes were compared, not only amongst themselves but, where possible, with recent observational analyses of the boundary-layer structure. Although the study identified shortcomings of the individual schemes (e.g., the GFS scheme), it fell short of advocating the use of a particular scheme. The authors concluded that the current inability to determine "the optimum scheme" had implications for the predictability of TC intensification.

Although it is clear from the above discussions that modeled TC structure and intensity predictions are known to be sensitive to PBL parameterization schemes, it is unclear why a particular scheme behaves differently when compared to another or what might be a case independent, optimal choice for improving TC numerical forecasts. To address these issues, we focused our efforts on the fundamental source of variability in the structure and intensity prediction in high resolution numerical models, namely, vertical eddy diffusivity. Specifically, in this work we studied the impacts of modifying Km (and Kh), consistent with the observed flight-level data from mature storms, on the structure and intensification of an idealized vortex within the framework of the HWRF system. We used the GFS scheme because of its simplicity to the TC forecasting problem and its use in NCEP operational models. To the best of our knowledge, this is the first time a synthesis of flight-level observations has been used as the basis to provide an improvement to the existing boundary layer parameterization scheme in a high resolution hurricane model. The study also provides a basic understanding of the influence of vertical diffusion on the size, structure, and subsequent intensification of modeled storms.

2. The HWRF Model, Configuration, and Physics

The HWRF system was developed at NOAA's National Weather Service (NWS)/NCEP to address the Nation's next generation hurricane forecast problems and became an operational track and intensity guidance tool in 2007. A version of this evolving system is available at the Development Testbed Center (DTC), National Center for Atmospheric Research (NCAR), in Boulder, Colorado, and the scientific documentation (Gopalakrishnan et al. 2010) is available at http://www.dtcenter.org/HurrWRF/users/docs/scientific_documents/__HWRF_final_2-2_cm.pdf.

An experimental version of the HWRF system (dubbed as HWRFX) was specifically adopted and developed at the Hurricane Research Division (HRD) of the Atlantic Oceanographic and Meteorological Laboratory (AOML) to study the intensity change problem at cloud-resolving scales (about 1-3 km). This modeling system is supported by NOAA's Hurricane Forecast Improvement Project (HFIP) and complements the operational HWRF system. HWRFX can be run both in real (Zhang et al. 2011; Yeh et al. 2011; Pattanayak et al. 2011) and idealized frameworks (Gopalakrishnan et al. 2011a). Until recently, we developed and tested new techniques with HWRFX that evaluated their potential to improve hurricane forecasts before they became formally adopted for use within HWRF. However, as the research and operational communities collaborated under the auspices of HFIP to improve TC intensity forecasts, we realized the need to merge the two systems. The merger of the experimental and operational systems, HWRFV3.2, was used in the current study.

. In this work, we used the triply-nested version of the HWRFV3.2 system. The model is configured with a coarse mesh of 27 km horizontal grid spacing covering about 50 x 50 degrees and two, two-way telescopic moving nests at 9 km covering about 15 x 15 degrees and 3 km covering about 5 x 5 degrees, respectively. There are 42 hybrid levels with at least 11 levels below the 850-mb level (approximately located at 33, 105, 189, 285, 396, 524, 671, 839 1030 1247 and 1493 m). Recently, HWRFX was used in an idealized framework to gain a fundamental understanding of the influence of horizontal grid resolution on the dynamics of hurricane vortex intensification in three dimensions (Gopalakrishnan et al. 2011a). We used the same ideal initialization in this work. Described in brief, the non-linear balance equation in the pressure-based sigma

coordinate system described in Wang (1995) was solved within the rotated latitude-longitude E-grid framework, where the mass field was obtained from the wind field. The calculations were performed on an f-plane centered at 15^0. The model was initialized with an axisymmetric cyclonic vortex of initial strength of 20 m s^{-1} with a radius of maximum wind of about 90 km, embedded in a uniform easterly flow of 4 m s^{-1}. The far field temperature and humidity were based on Jordan's Caribbean sounding (Gray et al. 1975). In all of the experiments, the sea surface temperature was set to 302 K, and no land was present anywhere in the domain.

The model physics options used in this study were configured as close as possible to the operational HWRF system. An extensive overview of the physics packages used in the HWRF system is provided in Gopalakrishnan et al. (2010) and Yeh et al. (2011) and only briefly discussed here. The Ferrier scheme (Ferrier et al. 2002) was used to provide latent heating to resolve the grid scale microphysical processes in the atmosphere, and the Simplified Arakawa and Schubert scheme, also known as the SAS scheme (Pan and Wu 1995; Hong and Pan 1998), was used to parameterize subgrid cumulus-cloud activity for the two domains at resolutions of 27 km and 9 km. The use of cumulus parameterization for a domain resolution of 3 km is a point of debate in operational models. Cumulus parameterizations in combination with the Ferrier microphysical scheme have been found to have some value in the operational Non-Hydrostatic Mesoscale Model (NMM) for scales down to about 3-5 km (Gopalakrishnan et al. 2011a). Consequently, we tested the entire set of simulations reported here with and without a cumulus parameterization scheme for the 3-km domain. We report the results of the simulations without the SAS scheme in the third nest. The GFDL long wave radiation scheme that follows the

simplified exchange method of Fels and Schwarzkopf (1975) and Schwarzkopf and Fels (1991) and the short-wave radiation of Lacis and Hansen (1974) were also used in the current study.

The HWRF system uses the GFDL surface layer parameterization scheme. Based on the Monin-Obukhov similarity theory, the parameterization scheme provides estimates[2] of the surface layer exchange coefficients, Cd and Ck, for further computation of the surface layer fluxes. Since the 2006 GFDL model upgrades, the Cd values computed in the scheme have provided estimates consistent with observations for both higher and lower wind speeds (Bender et al. 2007). However, largely due to uncertainties in the observations, Ck was left unchanged (Fig. 3 in Bender et al. 2007). Until the 2009 hurricane season, the HWRF system used the GFDL implementation of the surface layer scheme. However, based on more recent laboratory experiments (Haus et al. 2010) the upgraded operational HWRF system in 2010 used a function for roughness length for momentum, heat and moisture that produces a value of about 1.3×10^{-3} for Ck. Figures 1a and 1b provide an estimate of Cd and Ck, respectively, obtained from one of the simulations reported here. The simulated values obtained from the 72nd hour of the forecast representing a mature storm were compared with currently available observations. With the 2010 surface layer upgrades, we believe the HWRF system provides a reasonable parameterized estimate of the surface layer exchange coefficients within the range of the observational uncertainties.

[2] *In advanced numerical models, the exchange coefficients are a function of stability and the roughness lengths for momentum, heat, and moisture.*

The GFS boundary layer formulation (Hong and Pan 1996), which is the main topic of discussion in this study, was used to parameterize the flux transport and subsequent mixing in the atmosphere. In this scheme, the momentum eddy diffusivity is

$$Km = k\,(U_*/\Phi_m)\,Z\,\{\alpha(1 - Z/h)^2\}, \qquad (1)$$

where k is the von Karman constant (=0.4), U_* is the surface frictional velocity scale, Φ_m is the wind profile function evaluated at the top of the surface layer, Z is the height above the surface, and h is the depth of the turbulent PBL (also known as the mixed layer) that is determined based on the height above the ground at which the bulk Richardson number exceeds a critical value of 0.5. In the original formulation, which may be valid over land, α=1.0. In this study, we used a synthesis of observations from Zhang et al. (2011a,b) and conducted several sensitivity experiments by varying the value of α. However, since the differences were systematic only simulations of significance are reported in Table 1. Further, we evaluated the value of α that best provides estimates of the observed diffusivities and then studied the impacts of these changes on the structure and intensity changes of the ideal vortex. As discussed in Hong and Pan (1996), the eddy diffusivity for heat (and moisture), Kh, was computed from Km using the relationship of the Prandtl number. Finally, the numerical diffusivity along the horizontal direction was held fixed to a small background value in all the experiments. The input parameter that controls the lateral diffusion in the HWRF system is known as COAC (Gopalakrishnan 2011b), and this parameter was set to 0.7 in all domains. This is the smallest suggested value for the NMM dynamic core.

3. Results and Discussion

3.1 Methodology of Analysis of the Results

All simulations reported in Table 1 were run for 96 hours. The minimum mean sea-level pressure (MSLP) was well defined during the simulations and was used by the tracking algorithm to determine the center of the storm. Apart from the examination of the time traces for the minimum MSLP, maximum 10-m wind speeds in the inner core, and eddy diffusivities for momentum (Km) that were isolated from the raw hourly output on the native grid system of the inner moving nest at 3-km resolution, we further divided our investigation into two parts. These parts included (i) an axisymmetric analysis of the output from the 3 km inner moving nest following Gopalakrishnan et al. (2011a), where the influence of horizontal resolution and physics on the structure and intensity changes in TCs using a similar idealized framework were studied, and (ii) a simple examination of the basic gradient wind equations that involved an iterative solution of the coupled equations for the radial and tangential components of wind (Stull 2000; Montgomery and Smith 2008).

As illustrated in Zhang et al. (2001) and Gopalakrishnan et al. (2011a), it is convenient to discuss the axisymmetric inner-core dynamics in cylindrical coordinates (r, λ, z), where r is the distance from the center of the vortex, λ is the azimuthal angle, and z is the vertical height. The hourly output on the native moving grid from the model was transformed to the cylindrical polar height coordinate system. Any time averaging reported in the later part of this work was done after this transformation. Further, for the sake of analysis, we recast the horizontal equations of motion into tangential momentum, governing the primary circulation and radial components that govern the secondary circulation for the HWRF system. The governing equations are:

$$\frac{dv_\lambda}{dt} = -\frac{1}{\rho r}\frac{\partial p}{\partial \lambda} - \underbrace{\frac{u_r v_\lambda}{r} - fu_r}_{\text{Term A}} + D_{v\lambda} \qquad (2)$$

$$\frac{du_r}{dt} = -\underbrace{\frac{1}{\rho}\frac{\partial p}{\partial r} + \frac{v_\lambda v_\lambda}{r} + fv_\lambda}_{\text{Term B}} + D_{ur} \qquad (3)$$

$$\text{Where } \frac{d}{dt} = \frac{\partial}{\partial t} + u_r\frac{\partial}{\partial r} + \frac{v_\lambda}{r}\frac{\partial}{\partial \lambda} + w\frac{\partial}{\partial z} \qquad (4)$$

In equations 2, 3, and 4, u_r, v_λ, and w are, respectively, the radial, tangential, and vertical winds in the earth-relative transformed coordinate system, p is the pressure, and Dv_λ and Du_r are, respectively, the diffusion (or frictional force) terms in the tangential and radial directions. Equation 2 is related to the "spin up" of the vortex, and Term A is known as the generalized Coriolis term. Its significance to the "spin up" process is discussed later in the text. Equation 3 represents the net forcing related to the secondary circulation.

By assuming the radial pressure gradient force is in balance with the centripetal and Coriolis forces above the boundary layer and a bulk drag law at the lower boundary (i.e, $Km(dU_b/dz)= Cd\ M\ U_b$, where U_b denotes the horizontal component of wind in the slab boundary layer, and M represents the wind speed), for a slab boundary layer of mean thickness, δ, equations 2 and 3 reported in this work may be recast into the horizontal momentum equations 9 and 10 reported in Smith and Montgomery (2008). Apart from the analysis of simulation outputs reported in Table 1 and to provide additional insight on the relationship between the radial frictional forces (last term in equation 3), radial

acceleration, and subsequent inflow, this coupled system of equations for the momentum boundary layer was solved with an iterative procedure and used in our discussions (we refer to this system as a toy model).

3.2 Time Series of the Vortex Developments

Figure 2 provides a time history of the intensification of the inner nest at 3-km resolution for the control run (A100), α of 0.50 (A050), and α of 0.25 (A025), respectively, while Table 2 provides the storm statistics sampled from the entire life history of the storm. After an initial period of gestation, a period of rapid intensification is observed starting at about 12 hours for all three simulations and continuing almost up to 36 hours (Fig. 2a). During this time, the MSLP is reduced to 978 hPa in A100, 961 hPa in A050, and 948 hPa in A025. The MSLP at the end of the simulations are, respectively, 959 hPa, 946 hPa, and 925 hPa (Table 2). In addition, although the initial size of the radius of maximum winds for the storm in all three cases was set to 90 km, it is reduced rapidly during the model integration, with A025 producing the smallest inner core in the three cases (Fig. 2b). The minimum radius of maximum winds during 24-96 hours of the simulation for A100 was 31 km, whereas it was 16 km in A025 (Table 2). Figures 2c,d,e provide Hovemoller diagrams of the axisymmetric mean winds at a height of 10 m for A100, A050, and A025. Also, the maximum tangential wind speed in the storm during its lifetime for A100 was 51 m s^{-1}, whereas it was about 81 ms^{-1} for A025 (Table 2). Clearly, A025 produces the strongest inner core, as well as the smallest inner core[3]. Also notice that while the inner core in (Fig. 2 c,d,e) reaches a quasi steady state, the gale-forced wind keeps expanding consistent with the two spin up mechanisms discussed in Smith et

[3] As measured by the radius of azimuthally averaged maximum tangential wind at the first model level (about 30 m) in this study.

al. (2009) and verified in Gopalakrishnan et al. (2011a). The evolution of the MSLP is consistent with the evolution of the axisymmetric winds (Fig. 2a). We further analyzed the intensification process in light of these results. Gopalakrishnan et al. (2011a) provided an overview of the rapid intensification phase. In this study, we focus on the impact of the PBL diffusion on the behavior of the mature storm.

3.3 Comparison of Eddy Diffusivities with Observations

Figure 3 depicts the modeled variation of Km with wind speed for the control run (A100), α of 0.50 (A050), and α of 0.25 (A025), respectively. Flight-level observations from hurricanes Hugo and Allen presented in Zhang et al. (2011a) were compared with the modeled outputs at nearly the same height. Clearly consistent with the initial findings of Braun and Tao (2000), the original GFS scheme (A100) overestimates the values of Km. Nevertheless, more reasonable modeled estimates are produced after decreasing the α parameter. We trailed a string of values for α as small as 0.10 (not reported). The estimates produced in the A025 simulation, where Km was reduced to a quarter of its original value, provided the closest match with the observations (Fig. 3c). Reduction of vertical diffusion in the A050 and A025 simulations had a significant influence on the structure of the PBL and subsequent TC intensification process and will be discussed in the following section.

3.4 Structure and Intensification Process

Figure 4 shows the tangentially-averaged, 6-hourly time averaged, radius-height cross section of the secondary circulation centered around the 93rd hour of the simulations and represents the mean structure of a mature storm for the control run (A100), α of 0.50 (A050), and α of 0.25 (A025), respectively. As indicated by the vectors and contours in Fig. 4a, the circulation in the A100 simulation is characterized by a deep layer of radial inflow

almost more than a couple of kilometers deep[4] in the lower troposphere and a layer of intense outflow characterizing the upper-level divergence at about 14 km height (not shown for the sake of clarity). The rising branch of the secondary circulation, depicted by green contours and located in the eyewall region, slopes radially outward. A *very weak* outflow is observed above the shallow inflow layer due to the return flow. The model is able to reproduce the same features as reported in Gopalakrishnan et al. (2011a). However, a comparison with the available observational data from Zhang et al. (2011b) indicates that the simulated inflow layer depth is at least twice the thickness of that observed. Nevertheless, more reasonable modeled estimates are produced after decreasing the α parameter. A comparison between A100 with A050 and A025 (Figs. 4a,b,c) indicates a systematic reduction of the inflow depth with a decrease in Km (and Kh) and an increase in the strength of the radial winds. The inflow layer in A100 is about 2.0 km, while it is about 1.5 km in A050 and reduces to the observed value of about 1 km in A025. As the depth of the inflow layer decreases, the strength of the inflow increases. While the maximum radial wind in A100 is, on average, about 6-9 m s^{-1}, it is 9-15 m s^{-1} in A050 and 27-33 m s^{-1} in A025. The eyewall also shrinks in size. While the radius of maximum wind is 51 km in A100, it is 40 km in A050 and further reduces to 22 km in A025.

In a hypothetical situation where diffusivity is reduced to zero, radial acceleration in the boundary layer is negligible and the rings of air are in gradient wind balance (i.e., term B in equation 3), approximately conserving absolute angular momentum even above the shallow surface layer. However, vertical eddy diffusivity (Km) controls and modulates the radial frictional force (diffusion term in equation 3) and, subsequently, the

[4] *The depth of the inflow in this study was taken to be the height where the radial wind velocity is reduced to about 3 ms^{-1}. Significant inflow above the boundary layer is not uncommon (e.g., Willoughby 1979).*

radial acceleration and strength of the inflow, especially in the eyewall region above the surface layer, by creating or negating gradients in the mean flow. Figure 5 shows a tangentially averaged, 6-hourly time averaged, radius-height cross section of eddy diffusivity (Km) at 93 hours for (a) control (α=1), (b) Km reduced to half (α=0.50), and (c) Km reduced to a quarter (α=0.25). It is seen that the maximum turbulence and eddy diffusion are simulated in the eyewall region. Lorsolo et al. (2010), for the first time, reported estimates of turbulent kinetic energy in hurricanes using observations from airborne Doppler radar. They found that the strongest turbulence was generally located in convective regions, such as the eyewall, and that the mean vertical profiles of turbulent kinetic energy decreased sharply above the mixed layer. Lorsolo et al. (2010) also found that turbulent kinetic energy leveled off at a low magnitude for all regions outside the radius of maximum wind. These findings are consistent with the current study. Further, superposed in color (Fig. 5) are the forcing terms related to gradient wind imbalance within the boundary layer (i.e., term B in equation 3). Units of the forcing term are in m s^{-1} h^{-1}. We find that within the first 500 m above the ground level, between a radius of about 30-120 km where the effect of inflow is at its maximum, the eddy diffusivity (Km) has a maximum of 300 m^2s^{-1} for the α=1 case, 150-200 m^2s^{-1} for the α=0.5 case, and 50-100 m^2s^{-1} for the α=0.25 case. It may be noted that the Km values from flight-level data at approximately 450-500 m well match the α=0.25 case (Fig. 3). The α=0.25 run also clearly shows a maximum imbalance in the eyewall region. The winds are strongly sub-gradient (pressure gradient term dominates the centripetal force in equation 3) and, subsequently, lead to a stronger acceleration near the eyewall region. We also observe an overshoot of near surface inflow that leads to super gradient winds (Fig. 5c, indicated in

red), whereas large vertical diffusion (α=1) negates any possible gradient that might be created in the control run (Fig. 5a). *In other words, the weaker the frictional force in the mixed layer, the weaker the radial inflow*.

As mentioned in section 3.1, to further understand the influence of the inflow depth on the surface wind, a "toy model" was developed based on a simple balance/imbalance of forces along the horizontal direction in the PBL. Equations 2 and 3 reported in this work were recast into the horizontal momentum equations 9 and 10 reported in Smith and Montgomery (2008). However, for the Lagrangian analysis discussed here, we replaced the radial advection term on the left side in Smith and Montgomery (2008) with total time derivative terms and solved the coupled system moving forward in time with an iterative procedure reported in Stull (2003). We also neglected the effect of updrafts in this simple model. It should be noted that in few hundred iterations the model will achieve a steady state. We traced the hodographs during that process. Given the tangential winds above the slab boundary layer, the drag coefficient at the lower boundary, and the mean depth of the slab layer, the tangential winds within the slab layer adjust to a new state due to the changing balance between the pressure gradient and the Coriolis, centrifugal, and friction forces within the boundary layer. In the process, a radial inflow is created. It should be noted that in a slab model, the frictional force term (in equations 2 and 3) is parameterized by Cd M U_b/δ. The drag formulation was adopted from Smith and Montgomery (2008). Although depth averaged/slab models may not be a substitute for the height-resolving model discussed in Kepert (2010) or for more complex models such as HWRF, where the mixing and inflow layer depths evolve based on both the dynamics and thermodynamics in the model, as seen later in these discussions, the former class of

simple models may still be adopted to provide additional insight on the impacts of the diffusion term to the inflow. This is especially true for the Lagrangian trajectory analysis conducted here. An increase in the depth of diffusion, for instance, leads to a reduction in frictional force in the slab model and may be equivalent to producing a more diffusive boundary layer by increasing the eddy diffusivity (i.e., α=1 case). On the other hand, decreasing the depth of diffusion in the slab model is equivalent to increasing the frictional forces and, hence, the radial acceleration. For the hypothetical situation discussed earlier, where the eddy diffusivity was reduced to zero (i.e., alpha=0; not shown), although the air was in gradient wind balance above the surface layer, there would also be an infinite acceleration in the surface layer because the depth of the inflow becomes negligible. Fig. 6 a, b, and c provide the hodographs for different tangential winds (51, 64, and 81 ms^{-1}) that are representative of those obtained for a matured storm from the HWRF simulations for α=1, 0.50, and 0.25, respectively (Table 2). For each of these cases, Table 3 provides the list of sensitivity experiments performed with the slab model. The results obtained from these simple experiments are consistent with the discussions provided above on the role of eddy diffusivity and the radial diffusion term (in equation 3). In general, for a given tangential wind, the *weaker the frictional force, the weaker the inflow*. From a Lagrangian point of view (Fig. 6 a,b,c), the larger the frictional force, the larger the radial acceleration as measured by the size of radial displacement. The steady state values in Table 3 also indicate that the values of the inflow from the slab model under different conditions are consistent with those from HWRF simulations for α=1, 0.50, and 0.25, respectively. While there is large variability in the steady state values, it is again seen that for a prescribed tangential wind, stronger

frictional force (lower but non-zero vertical diffusion) leads to stronger inflow and vice-versa.

A reduction in vertical eddy diffusivity (Km and Kh) and the subsequent increase in the strength of the radial inflow have a significant influence on the structure and intensity of the TC. Figure 7 provides a Hovemoller diagram of the tangentially-averaged, 6-hourly time averaged radial component of velocity (in m s^{-1}). Superposed on the contour lines is the generalized Coriolis term (i.e., Term A in equation 2) *with the addition of a frictional effect* from equation 2 for the HWRF runs with (i) α=1 (A100), (ii) α=0.5 (A050), and (iii) α=0.25 (A025) runs at the 30-m level. The blue end of the spectrum represents tangential acceleration ("spin up"), and the red end of the spectrum represents deceleration. A comparison between Figs. 7a,b,c clearly indicates that the increase in inflow speed is coupled with the increase in generalized Coriolis and subsequent increase in tangential acceleration *despite friction* (equation 2). Montgomery and Smith and their colleagues used MM5 at a resolution of about 1.67 km to examine the basic process of intensification in an idealized vortex (see Montgomery and Smith 2011 for a summary). These studies showed that the axisymmetric aspects of intensification involve not only the convergence of absolute angular momentum above the boundary layer but also the convergence of absolute angular momentum within the boundary layer. There is no significant difference between the inflow above the PBL for A100, A050, and A025 (Fig. 4). However, it is the systematic increases to the strength of the inflow within the PBL that results in noticeable differences in the "spin up" processes.

It should be noted that spin up of the primary circulation (tangential winds) in a hurricane would cease to exist without eyewall convection. As explained in Gopalakrishnan et al. (2011a), convection is the main agent that transfers higher-θ_e air from the ocean surface to the upper troposphere (see Plate 1b in Emanuel 2003 for a classic view of this transport). The radial gradient of θ_e during the initial stage of the storm initiates subsidence. Subsidence is enhanced with the formation of a well-defined warm core and this, in turn, leads to a strengthening of the storm at a subsequent time. The warmer the core, the deeper the pressure and the stronger the wind at the surface.

Figure 8 provides the Hovemoller diagram of the tangentially-averaged, 6-hourly time averaged radial θ_e at the 30-m level for the HWRF runs with (i) α=1 (A100), (ii) α=0.5 (A050), and (iii) α=0.25 (A025). The region of vertical motion exceeding the 0.2 m s^{-1} contour line at the top of the boundary layer is shown to indicate the approximate region of eyewall convection. Cram et al. (2007) studied the transport and mixing characteristics of a large sample of air parcels from Hurricane Bonnie (1998). He found that a portion of the low-level inflow from the hurricane bypassed the eyewall to enter the eye, and this air both replaced the mass of the low-level eye and lingered for a sufficient time (order 1 h) to acquire enhanced entropy characteristics through its interaction with the ocean beneath the eye, which enhanced the efficiency of the hurricane heat engine (Emanuel 1986). A comparison between Figs. 8a,b,c illustrates that in addition to the "spin up" of the primary circulation (Fig. 7), the enhanced strength of the cross-isobaric flow (Fig. 4 and 5) provides a mechanism for increased entropy within the boundary layer. Although the surface latent heat fluxes (and enthalpy) were reduced in A025 (not shown), the enhanced

enthalpy caused by advection of moisture and heat above the surface layer was sufficient to produce a stronger hurricane.

Figure 9 provides a Hovemoller diagram of the tangentially averaged, 6-hourly time averaged radial component of velocity (in m s^{-1}). Superposed on the contour lines in colored shading is the net radial forcing term *including radial friction* from the governing equation for the secondary circulation (equation 3) of the HWRF runs with (i) α=1, (ii) α=0.5, and (iii) α=0.25 runs at the 30-m level. The blue end of the spectrum represents radial acceleration (convergence), and the red end of the spectrum represents deceleration within the inner eyewall region. Units of the net radial forcing term are in m s^{-1} h^{-1}. As indicated in Fig. 9a (and 5a), the PBL and eyewall regions are characterized by imbalances in the gradient wind. These results are comparable with those of Gopalakrishnan et al. (2011a). However, it should be noted that the strength of the agradient forcing used in that study had to be rescaled for the current study because of the significant increase in the strength of the inflow, as well as the agradient forcing terms for the other runs in Table 1. The following points are worth noting:

- The evolution of a mature TC occurs through cooperative interaction between the primary and secondary circulations (Ooyama, 1969, 1982). The larger the departure from the gradient wind in the PBL caused by increased radial frictional forces and, subsequently, the spin-up process discussed in the above section (refer to equations 2 and 3), the larger the acceleration in the eyewall and deceleration within the eye (equation 3). In an experiment with reduced drag, Montgomery et al. (2010) demonstrated that rapid acceleration of the inflowing air causes a greater agradient force and, hence, is converged farther

inward before rising out of the boundary layer and ascending into the eyewall updraft. While decreased drag caused convergence farther inward in their study (see Fig. 2, Montgomery et al. 2010), the strength of the inflow modulated by vertical eddy diffusion and the subsequent "spin up" *within the boundary layer* led to the imbalance and subsequent acceleration (and radial convergence) in the current study. Clearly for A025, the radial acceleration within the boundary layer was so strong (Fig. 9c) that a radial jet of 3 m s^{-1} was produced at about 1-1.5 km above the surface (Fig. 4c), consistent with the studies of Smith and Montgomery and coworkers (e.g., Smith et al. 2009; Montgomery et al. 2010), as well as other recent findings (Bell and Montgomery 2008).

- It is important to note that as the air is converged farther inward towards the eye in A100, A050, and A025 (Fig. 9), the size of the inner core, as defined here by the radius of maximum wind, decreases. For instance, while the radius of the maximum wind for a mature storm is about 51 km for A100 (Fig. 4a), it is reduced to about 40 km in A050 (Fig. 4b) and to about 22 km in A025 (Fig. 4c).

4. Sensitivity Experiments

A good review of the external factors that may control the size of the storm, both in terms of the inner core and spiral rainbands and the diabatic heating outside the eyewall region, is provided in Xu and Wang (2010). From this study, it appears that the initial size of the storm, as well as the environmental relative humidity, may have some

sensitivity on the inner core in the context of the results discussed above. Table 1 provides an overview of these sensitivity experiments (number 4 to 12).

Figure 10 depicts the Hovemoller diagram of the axisymmetric mean wind at 10 m (in color). Superposed are the contours of tangentially averaged, 6-hourly time averaged radial components of velocity (in m s^{-1}) at the 30-m level (i.e., first model level) for the HWRF runs with an initial radius of maximum wind set to 120 km (top row) and 60 km (middle row) and for (i) α=1 (B100 and S100), (ii) α=0.5 (B050 and S050), and (iii) α=0.25 (B025 and S025) runs (Table 1). The bottom row illustrates the importance of the environmental relative humidity for the three α values (RHA100, RHA050, and RHA025 in Table 1). Several features are worth noting:

- A comparison between B100, B050, and B025, or S100, S050, and S025, indicates that the TC inner core size is critically dependent on the initial vortex size. A larger initial storm evolves to become a larger storm, and an initially smaller storm evolves to become even smaller. While the radius of maximum wind was on the order of 71 km at 96 hours in B100 (Fig. 10a), the minimum size was as small as 13 km around 96 hours in S025 (Fig. 10f).
- Xu and Wang (2010) found that strong outer winds in a storm with a larger initial size led to large entropy fluxes and to a large radial extent outside the eyewall, favoring the development of active spiral rainbands and, subsequently, larger (area wise) radial inflow and accelerating tangential winds outside the eyewall. These factors also led to an outward expansion of the tangential wind fields. On the contrary, based on the same argument, an initially small vortex

remained weak and small in this study. The results in Fig. 10 are consistent with those from Xu and Wang (2010).

- More importantly, within the context of the current study, a comparison between B100, B050, and B025 (Figs. 10a,b,c) indicates that the eddy diffusivity has a significant influence on this class of big storms. There is a systematic increase in the strength of the inflow and, subsequently, the strength of the storm (Table 2) with the decrease in eddy diffusivity very similar to A100, A050, and A025 (Figs. 7 and 9). Initially smaller storms (S100, S050, and S025; Figs. 10d,e,f) show the same trend, indicating that the findings discussed in the earlier part of this study are not altered by some of the external factors that may affect storm size.
- A comparison between Figs. 2c,d,e with Figs. 10g,h,i in terms of wind speed at the 10-m level shows that intensification of the TC inner core is initially stunted in a dryer environment. However, the storm rapidly intensifies after 40 hours. Further, a comparison between simulations RHA100, RHA050, and RHA025 (Figs. 10g,h,i) indicates that there is a systematic increase in the strength of the inflow and, subsequently, in the strength of the storm (also refer to Table 2) with the decrease in eddy diffusivity very similar to A100, A050, and A025.

5. Summary and Conclusions

Through a series of numerical experiments using the HWRF system in an idealized framework, we demonstrate and document some very large impacts of vertical diffusion on the structure and subsequent intensification of TCs. Such sensitivities have been noticed in numerical models, especially when different PBL parameterization

schemes are used. However, here we try to address and explain the fundamental source of variability in TC intensity and structure prediction that may arise due to vertical diffusion. The GFS PBL scheme was used to understand the influence of vertical diffusion on the dynamics of TCs. Flight-level data collected by a NOAA WP-3D research aircraft during the eyewall penetration of category 5 Hurricane Hugo (1989) at an altitude of about 450-500 m (Marks et al. 2008) and Hurricane Allen (1980) (Marks 1985) were used as the basis to best match the modeled vertical eddy diffusivities with wind speed. The following are the salient results from this study:

- Reduction of eddy diffusivities, Km (and Kh), to 25% of its original value produces reasonable diffusion coefficients consistent with observations for all wind speeds ranging from about 10 m s^{-1} to about 60 m s^{-1} in the GFS scheme.
- Reduction of Km has a significant influence on the structure, size, and evolution of the vortex. With Km set to 25% of its original value, the depth of the inflow layer is reduced from ~2 km to about 1 km, again, more consistent with the observations.
- Larger diffusion negates the gradients between the surface layer and the PBL, leading to weaker frictional forces and weaker inflow. On the contrary, a reduction in diffusion leads to a reduction in the dissipation of angular momentum in the PBL (i.e., an increase of frictional forces in the equations of motion) which, in turn, leads to enhanced PBL inflow, enhanced spin-up in PBL, enhanced convergence of moisture in PBL, enhanced convection in the eyewall and, subsequently, enhanced feedback to the PBL inflow and a stronger hurricane.

- The influence of the frictional forces on the inflow is well supported by results obtained from a simple slab model for the hurricane boundary layer.
- Stronger acceleration in the inflow also leads to convergence farther inward before rising out of the boundary layer and ascending into the eyewall updraft and, consequently, a smaller storm in terms of the eyewall.
- Neither the initial vortex size nor the environmental relative humidity, which are known external factors that control the size of the storm, affect the above results.
- The structure of the PBL and the axisymmetric "spin up" of the idealized vortex discussed here appear to be more consistent with some of the observational (Zhang et al. 2011a,b) and theoretical modeling works (Montgomery and Smith 2011) that use a different parameterization scheme for vertical diffusion (e.g., Nolan et al. 2009a,b) when Km (and Kh) in the GFS scheme is reduced to 25% of its original value.

It should be mentioned that the current study is limited to numerical weather prediction models (NWP) for TCs in which turbulence is parameterized in terms of admittedly simplified parameters, rather than requiring such effects to be consequences of dynamics of the system (e.g. direct numerical simulations and Large Eddy Simulations). We also choose the GFS scheme because of the simplicity involved in its evaluation with available observations. Higher order PBL closure schemes such as the Turbulence Energy Closure (TKE) scheme require an evaluation of mixing length. An evaluation of the TKE parameterization scheme within the HWRF system will be performed in a follow up study. The current study establishes the basis for such forthcoming efforts.

Bryan and Rotunno (2009) used an axisymmetric, non-hydrostatic numerical model to evaluate the maximum possible intensity of tropical cyclones. At a resolution of 1 km or less, the authors found significant sensitivity to the specification of turbulence intensity in their model. In particular, the authors concluded that the lateral diffusion in the model limits maximum intensity because it reduces the radial gradient of angular momentum, and turbulence also reduces radial gradients of θe (scalar). While other studies of both real and ideal cases show significant sensitivity to lateral diffusion (Gopalakrishnan et al. 2011b; Bao et al. 2011), we fixed the coefficient of lateral diffusion to a minimum value recommended for the non-hydrostatic dynamic core (Janjic 1990) in the current work and instead varied the vertical diffusivity which also showed a sensitive dependence on the structure and intensity changes in the TCs. Unlike the vertical diffusion process which is parameterized in terms of physical effects, the application of lateral diffusion in atmospheric models in general has always been a subject of debate since it is not clear to what extent one can model horizontal diffusion. Although it is not feasible to run direct numerical simulations even to understand the turbulence structure of TC at this time, we believe that the use of observations to improve parameterization scheme in NWP applications especially for TC is a realizable goal. Recent studies from Zhang et al. (2012) also provide an estimate of horizontal eddy diffusivity and mixing length in low-level region of intense hurricane. We are in the process of evaluating both the vertical and horizontal diffusivity in the HWRF system for real cases, as well.

Finally, the structure and intensification of modeled TC are known to be sensitive to different parameterization schemes. A complementary study by Bao et al. (2011)

discusses the sensitivity of the structure and intensification in an idealized developing TC to various physics parameterization schemes in the HWRF system including microphysical and radiation parameterization schemes. The results presented here and in Bao et al. (2011) highlight the need for the research community to use structural metrics and better structural observations in its model evaluations to improve numerical models.

Acknowledgments:

The authors acknowledge funding from NOAA's Hurricane Forecast Improvement Project that supported this work. We acknowledge the contributions from Dr. Kao-San Yeh on the HWRF developmental efforts. Thanks are also due to Prof.Mike Montgomery, Drs. Robert Rogers and Young Kwon for providing a thorough internal review and insightful comments that led to significant improvements of the original manuscript. Thanks are due to Ms. Gail Derr for offering editorial support and to Mr. Arthur Eiserloh, a summer intern at NOAA who helped the primary author with the coding of the simple gradient wind equation that provided additional insights to this work. All the three reviewers and the editor, Prof.Robert Houze offered some insightful comments that greatly improved the manuscript. We acknowledge their efforts, as well.

References:

Anthes, R. A., and S. W. Chang, 1978: Response of the hurricane boundary layer to changes of sea-surface temperature in a numerical model. *J. Atmos. Sci.*, **35**, 1240-1255.

Bao, J.-W., S. G. Gopalakrishnan, S. A. Michelson, F. D. Marks, and M. T. Montgomery, 2011: Sensitivity of tropical cyclone structure and wind-pressure relationships to physics representations in the HWRFX model (*Mon. Wea. Rev., in press*).

Bell, M. M., and M. T. Montgomery, 2008: Observed structure, evolution, and potential intensity of category 5 Hurricane Isabel (2003) from 12-14 September. *Mon Wea. Rev.*, **136**, 2023-2046.

Bender, M. A., I. Ginis, R. E. Tuleya, B. Thomas, and T. Marchok, 2007: The operational GFDL coupled hurricane-ocean prediction system and a summary of its performance. *Mon. Wea. Rev.*, **135**, 3965-3989.

Black, P. G., and Coauthors, 2007: Air–sea exchange in hurricanes: Synthesis of observations from the Coupled Boundary Layer Air–Sea Transfer Experiment. *Bull. Amer. Meteor. Soc.*, **88**, 357–374.

.

Braun, S. A., and W.-K. Tao, 2000: Sensitivity of high-resolution simulations of Hurricane Bob (1991) to planetary boundary layer parameterizations. *Mon. Wea. Rev.*, **128**, 3941–3961.

Bryan, G. H., and R. Rotunno, 2009: The maximum intensity of tropical cyclones in axisymmetric numerical model simulations. *Mon. Wea. Rev.*, **137**, 1770-1789.

Cram, T. A., J. Persing, M. T. Montgomery, and S. A. Braun, 2007: A Lagrangian trajectory view on transport and mixing processes between the eye, eyewall, and environment using a high-resolution simulation of Hurricane Bonnie (1998). *J. Atmos. Sci.*, **64**, 1835–1856.

Donelan, M. A., B. K. Haus, N. Reul, W. J. Plant, M. Stiassnie, H. C. Graber, O. B. Brown, and E. S. Saltzman, 2004: On the limiting aerodynamic roughness of the ocean in very strong winds. *Geophys. Res. Lett.*, **31**, L18306, doi:10.1029/2004GL019460.

Emanuel, K. A., 1986: An air-sea interaction theory for tropical cyclones. Part I: Steady-state maintenance. *J. Atmos. Sci.*, **43**, 585–604.

Emanuel, K. A., 1995: Sensitivity of tropical cyclones to surface exchange coefficients and a revised steady-state model incorporating eye dynamics. *J. Atmos. Sci.*, **52**, 3969-3976.

Emanuel, K. A., 2003: A century of scientific progress. Hurricane! Coping with Disaster, R. Simpson, R. Anthes, and M. Garstang, Eds., Special Publication, Vol. 55, Amer. Geophys. Union, 177–216.

Fels, S. B., and M. D. Schwarzkopf, 1975: The simplified exchange approximation: A new method for radiative transfer calculations. *J. Atmos. Sci.*, **32**, 1475–1488.

Ferrier, B. S., Y. Lin, T. Black, E. Rogers, and G. DiMego, 2002: Implementation of a new grid-scale cloud and precipitation scheme in the NCEP Eta model. *Preprints, 15th Conference on Numerical Weather Prediction, San Antonio, TX, Amer. Meteor. Soc.*, 280-283.

Gopalakrishnan, S., Q. Liu, T. Marchok, D. Sheinin, N. Surgi, R. Tuleya, R. Yablonsky, and X. Zhang, 2010: Hurricane Weather and Research and Forecasting (HWRF) model scientific documentation. L. Bernardet, Ed., 75 pp.

Gopalakrishnan, S. G., F. D. Marks, X. Zhang, J.-W. Bao, K.-S. Yeh, and R. Atlas, 2011a: The experimental HWRF system: A study on the influence of horizontal resolution on the structure and intensity changes in tropical cyclones using an idealized framework. *Mon. Wea. Rev.*, **139**, 1762-1784.

Gopalakrishnan, S. G., S. Goldenberg, T. Quirino, F. D. Marks, X. Zhang, K.-S. Yeh, R. Atlas, and V. Tallapragada, 2011b: Towards improving high-resolution numerical hurricane forecasting: Influence of model horizontal grid resolution, initialization, and physics. *Wea. Forecasting* (in press).

Gray, W. M., E. Ruprecht, and R. Phelps, 1975: Relative humidity in tropical weather systems. *Mon. Wea. Rev.*, **103**, 685-690.

Haus, B. K., D. Jeong, M. A. Donelan, J. A. Zhang, and I. Savelyev, 2010: Relative rates of sea-air heat transfer and frictional drag in very high winds. *Geophys. Res. Lett.*, **37**, L07802, doi:10.1029/2009GL042206.

Hong, S.-Y., and H.-L. Pan, 1996: Nonlocal boundary layer vertical diffusion in a medium-range forecast model. *Mon. Wea. Rev.*, **124**, 2322-2339.

Hong, S.-Y., and H.-L. Pan, 1998: Convective trigger function for a mass-flux cumulus parameterization scheme. *Mon. Wea. Rev.*, **129**, 1164-1178.

Janjic, Z. I., 1990: The step–mountain coordinates: Physical package. *Mon. Wea. Rev.*, **118**, 1429–1443.

Kepert, J. D., 2001: The dynamics of boundary layer jets within the tropical cyclone core. Part I: Linear theory. *J. Atmos. Sci.*, **58**, 2469–2484.

Kepert, J.D., 2010 Comparing slab and height-resolving models of the tropical cyclone boundary layer. Part I: Comparing the simulations. *Quart. J. Roy. Meteor. Soc.*, **136**, 1689-1699,

Kurihara, Y., and R. E. Tuleya, 1974: Structure of a tropical cyclone developed in a three-dimensional numerical simulation. *J. Atmos. Sci.*, **31**, 893–919.

Lacis, A. A., and J. E. Hansen, 1974: A parameterization for the absorption of solar radiation in the earth's atmosphere. *J. Atmos. Sci.*, **31**, 118–133.

Large, W. G., and S. Pond, 1981: Open ocean momentum flux measurements in moderate to strong winds. *J. Phys. Oceanogr.*, **11**, 324–336.

Lorsolo, S., J. Zhang, F.D.Marks, J. F. Gamache, 2010: Estimation and Mapping of Hurricane Turbulent Energy Using Airborne Doppler Measurements, *Mon. Wea. Rev*., **138**, 3656–3670)

Malkus, J. S., and H. Riehl, 1960: On the dynamics and energy transformations in steady-state hurricanes. *Tellus*, **12**, 1-20.

Marks, F. D., 1985: Evolution of the structure of precipitation in Hurricane Allen (1980).*Mon. Wea. Rev.*, **113**, 909-930.

Marks, F. D., P. G. Black, M. T. Montgomery, and R. W. Burpee, 2008: Structure of the eye and eyewall of Hurricane Hugo (1989). *Mon. Wea. Rev.*, **136**, 1237–1259.

Montgomery, M. T., R. K. Smith, and S. Nguyen, 2010: Sensitivity of tropical cyclone models to the surface drag coefficient. *Quart. J. Roy. Meteor. Soc.*, **136**, 1945-1953.

Montgomery, M. T., and R. K. Smith, 2011: Paradigms for tropical-cyclone intensification. *Quart. J. Roy. Meteor. Soc.*, **137**, 1-31.

Moon, I.-J., T. Hara, I. Ginis, S. E. Belcher, and H. Tolman, 2004a: Effect of surface waves on air–sea momentum exchange. Part I: Effect of mature and growing seas. *J. Atmos. Sci.,* **61**, 2321–2333.

Moon, I.-J., I. Ginis, and T. Hara, 2004b: Effect of surface waves on air–sea momentum exchange. Part II: Behavior of drag coefficient under tropical cyclones. *J. Atmos. Sci.,* **61**, 2334–2348.

Nolan, D. S., J. A. Zhang, and D. P. Stern, 2009a: Evaluation of planetary boundary layer parameterizations in tropical cyclones by comparison of in-situ data and high-resolution simulations of Hurricane Isabel (2003). Part I: Initialization, maximum winds, and outer core boundary layer structure. *Mon. Wea. Rev.*, **137**, 3651–3674.

Nolan, D. S., J. A. Zhang, and D. P. Stern, 2009b: Evaluation of planetary boundary layer parameterizations in tropical cyclones by comparison of in-situ data and high-resolution simulations of Hurricane Isabel (2003). Part II: Inner core boundary layer and eyewall structure. *Mon. Wea. Rev.*, **137**, 3675–3698.

Ooyama, K. V., 1969: Numerical simulation of the life cycle of tropical cyclones. *J. Atmos. Sci.,* **26**, 3-40.

——, 1982: Conceptual evolution of the theory and modeling of the tropical cyclone. *J. Meteor. Soc. Japan*, **60**, 369–379.

Pan, H.-L., and J. Wu, 1995: Implementing a mass flux convection parameterization package for the NMC medium-range forecast model. NMC Office Note, No. 409, 40 pp. (available from NCEP, 5200 Auth Road, Washington, DC 20233).

Pattanayak, S., U. C. Mohanty, and S. G. Gopalakrishnan, 2011: Simulation of very severe Cyclone Mala over Bay of Bengal with HWRF modeling system. *J. Natural Hazards (Published online: June 9, 2011).*

Powell, M. D., P. J. Vickery, and T. Reinhold, 2003: Reduced drag coefficient for high wind speeds in tropical cyclones. *Nature*, **422**, 279-283.

Rosenthal, S. L., 1962: A theoretical analysis of the field motion in the hurricane boundary layer. National Hurricane Research Project, Report No. 56, US Dept of Commerce (available from NOAA/AOML, Hurricane Research Division, Miami, FL 33149-1026).

Schwarzkopf, M. D., and S. Fels, 1991: The simplified exchange method revisited: An accurate, rapid method for computation of infrared cooling rates and fluxes. *J. Geophys. Res.*, **96**, 9075-9096.

Smith, R. K., 1968: The surface boundary layer of a hurricane. *Tellus,* **20**, 473–483.

Smith, R. K., 2003: A simple model of the hurricane boundary layer. *Quart. J. Roy. Meteor. Soc.*, **129**, 1007–1027.

Smith, R. K., and S. Vogl, 2008: A simple model of the hurricane boundary layer revisited. *Quart. J. Roy. Meteor. Soc.*, **134**, 337–351.

Smith, R. K., and M. T. Montgomery, 2008: Balanced boundary layers used in hurricane models. *Quart. J. Roy. Meteor. Soc.*, **134**, 1385-1395.

Smith, R. K., M.T.Montgomery, and N. V. Sang, 2009: Tropical cyclone spin-up revisited. *Quart. J. Roy. Meteor. Soc.*, **135**, 1321–1335.

Smith, R. K., and G. L. Thomsen, 2010. Dependence of tropical-cyclone intensification on the boundary-layer representation in a numerical model. *Quart. J. Roy. Meteror. Soc.*, **136**, 1671-1685.

Stull, R. B., 2000: *Meteorology for Scientists and Engineers*. Second Edition, Brooks/Cole, Thomson Learning, Pacific Grove, 502 pp.

Tuleya, R. E., and Y. Kurihara, 1978: A numerical simulation of the landfall of tropical cyclones. *J. Atmos. Sci.*, **35**, 242-257.

Wang Y., 1995: On an inverse balance equation in sigma-coordinates for model initialization. *Mon. Wea. Rev.*, **123**, 482-488.

Willoughby, H. E., 1979: Forced secondary circulations in hurricanes. *J. Geophys. Res*., **84**, 3173-3183.

Xu, J., and Y. Wang, 2010: Sensitivity of the simulated tropical cyclone inner-core size to the initial vortex size. *Mon. Wea. Rev*., **138**, 4135-4157.

Yeh, K.-S., X. Zhang, S. Gopalakrishnan, S. Aberson, R. Rogers, F. D. Marks, and R. Atlas, 2011: Performance of the experimental HWRF in the 2008 hurricane season. *J. Natural Hazards (Published online: March 24, 2011).*

Zhang, D.-L., Y. Liu, and M. K. Yau, 2001: A multiscale numerical study of Hurricane Andrew (1992). Part IV: Unbalanced flows. *Mon. Wea. Rev.*, **129**, 92-107.

Zhang, J., 2007: An airborne investigation of the atmospheric boundary layer structure in the hurricane force wind regime. *Doctoral Dissertation*, University of Miami, 149 pp.

Zhang, J. A., P. G. Black, J. R. French, and W. M. Drennan, 2008: First direct measurements of enthalpy flux in the hurricane boundary layer: The CBLAST results. *Geophys. Res. Lett.*, **35**, L14813, doi:10.1029/2008GL034374.

Zhang, J. A., F. D. Marks, M. T. Montgomery, and S. Lorsolo, 2011a: An estimation of turbulent characteristics in the low-level region of intense Hurricanes Allen (1980) and Hugo (1989). *Mon. Wea. Rev*., **139**, 1447-1462.

Zhang, J. A., R. F. Rogers, D. S. Nolan, and F. D. Marks, 2011b: On the characteristic height scales of the hurricane boundary layer. *Mon. Wea. Rev.,* **139**, 2523-2535.

Zhang, J. A. and M. Montgomery, 2011; Observational estimates of the horizontal eddy diffusivity and mixing length in the low-level region of intense hurricanes (In press, Journal of the Atmospheric Sciences)

Zhang, X., T. S. Quirino, S. Gopalakrishnan, K.-S. Yeh, F. D. Marks, and S. B. Goldenberg, 2011: HWRFX: Improving hurricane forecasts with high resolution modeling. *Comput. Sci. Eng.,* **13**, 13-21.

Figure Legends

Fig. 1. The variation of (a) drag coefficient (C_d) and (b) heat and moisture exchange coefficient (C_k) with 10-m wind speeds; high resolution HWRF model with 2010 upgrades (thick gray dots) from the control experiment (for α=1 in Table 1) compared with data from Large and Pond (1981), Powell et al. (2003), Donelan et al. (2004), Black et al. (2007), Zhang et al. (2008), and Haus et al. (2010).

Fig 2. Time history of the intensification process in an idealized storm for the three simulations provided in Table 1: (a) minimum mean sea level pressure in hPa, (b) radius of maximum wind at the first model level; Hovemoller diagram of the axisymmetric mean wind at a height of 10 m for (c) baseline simulation (α=1), (d) Km reduced to half (α=0.50), and (e) Km reduced to a quarter (α=0.25).

Fig. 3. The variation of the eddy diffusivity coefficient, Km, with 10-m wind speeds; high resolution HWRF model outputs from the (a) control experiment (α=1), (b) Km reduced to half (α=0.50), and (c) Km reduced to a quarter (α=0.25) compared with data from Zhang et al. (2011a).

Fig. 4. Tangentially averaged, 6-hourly time averaged, radius-height cross-section of the secondary circulation at 93 hours for (a) control (α=1), (b) Km reduced to half (α=0.50), and (c) Km reduced to a quarter (α=0.25). The black solid contour indicates the inflow, and the magenta contours show the outflow of the radial wind component (in m s^{-1}). Inflow is also shaded in colors. Only the lower 10 km has been expanded for convenience. The vertical velocity (in m s^{-1}) is shown by contour lines with updrafts indicted by green and weak subsidence indicated by yellow. Because the distribution of vertical velocity is skewed, please note that the scales are unequally spaced. For convenience, the vector field obtained that compounded the tangentially averaged vertical and the radial velocity components is also provided here. Presented in purple color are the estimates of the inflow layer depth from Zhang et al. (2011b).

Fig 5: Tangentially averaged, 6-hourly time averaged, radius-height cross section of eddy diffusivity (Km) at 93 hours for (a) control (α=1), (b) Km reduced to half (α=0.50), and (c) Km reduced to a quarter (α=0.25). Superposed in color are the forcing terms related to gradient wind imbalance within the boundary layer (i.e., term B in equation 3). Units of the forcing term are in m s^{-1} h^{-1}. The inflow is shown in the green background contours. For convenience, the vector field that compounded the tangentially averaged vertical and the radial velocity components is also provided. For the sake of clarity, only the first 3 km above the ground is displayed.

Fig 6: Hodographs obtained for different tangential winds (51, 67, and 84 ms^{-1}) from a simple slab model that was used to provide additional insights on the imbalance of forces

within the boundary layer. For each vortex, three boundary layer heights were used, namely, 1000 m (baseline), 600 m (strong frictional force), and 1400 m (weak frictional force).

Fig. 7. Hovemoller diagram of the tangentially averaged, 6-hourly time averaged radial component of velocity (in ms^{-1}). Superposed on the contour lines is the generalized Coriolis term (i.e., Term A in equation 2 in text) *with the addition of a frictional effect* shaded in color for the HWRF runs with (i) α=1, (ii) α=0.5, and (iii) α=0.25 runs at the 30-m level. The blue end of the spectrum represents tangential acceleration (contributing towards the "spin up"), and the red end of the spectrum represents deceleration within the inner eyewall region. Units of the forcing term are in $m\ s^{-1}\ h^{-1}$.

Fig. 8. Provides the Hovemoller diagram of the tangentially averaged, 6-hourly time averaged θ_e at the 30-m level for the HWRF runs with (i) α=1 (A100), (ii) α=0.5 (A050), and (iii) α=0.25 (A025). The region of vertical motion exceeding the 0.2 $m\ s^{-1}$ contour line at the top of the boundary layer is shown to indicate the approximate region of eyewall convection.

Fig. 9. Hovemoller diagram of the tangentially averaged, 6-hourly time averaged radial component of velocity (in $m\ s^{-1}$). Superposed on the contour lines in shaded color is the net radial forcing term *including radial friction* in the governing equation for the secondary circulation (equation 2) for the HWRF runs with (i) α=1, (ii) α=0.5, and (iii) α=0.25 runs at the 30-m level. The blue end of the spectrum represents radial acceleration (convergence), and the red end of the spectrum represents deceleration within the inner eyewall region. Units of the net radial radial forcing term are in $m\ s^{-1}\ h^{-1}$.

Fig. 10. Hovemoller diagram of the axisymmetric mean winds ($m\ s^{-1}$) at a height of 10 m. Contour lines representing the tangentially averaged, 6-hourly time averaged radial component of velocity (in $m\ s^{-1}$) at 30-m level are superposed. Top row (a), (b), and (c) are sensitivity experiments for an initially big vortex (experiments 4, 5, and 6 in Table 1). Middle row (c), (d), and (e) are sensitivity experiments for initially small vortex (experiments 7, 8, and 9 in Table 1) and bottom row (f), (g), and (h) are sensitivity experiments in which the relative humidity of the large scale environment was reduced to about 50% from the baseline Jordan sounding. The radius of the initial vortex size for the experiments illustrated in the bottom row (f, g, and h) was set to the base value, i.e., 90 Km (Table 1).

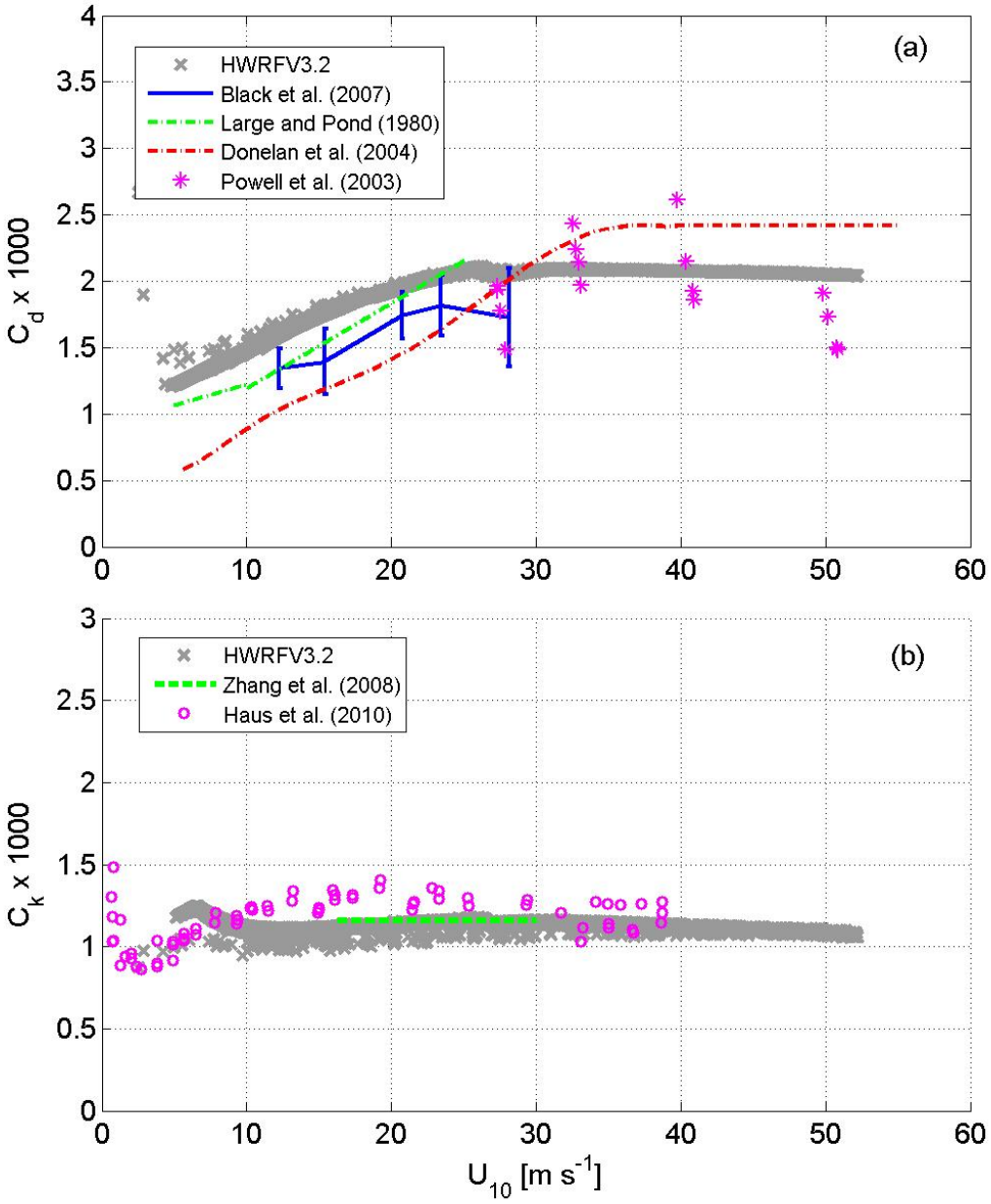

Fig. 1. The variation of (a) drag coefficient (C_d) and (b) heat and moisture exchange coefficient (C_k) with 10-m wind speeds; high resolution HWRF model with 2010 upgrades (thick gray dots) from the control experiment (for α=1 in Table 1) compared with data from Large and Pond (1981), Powell et al. (2003), Donelan et al. (2004), Black et al. (2007), Zhang et al. (2008), and Haus et al. (2010).

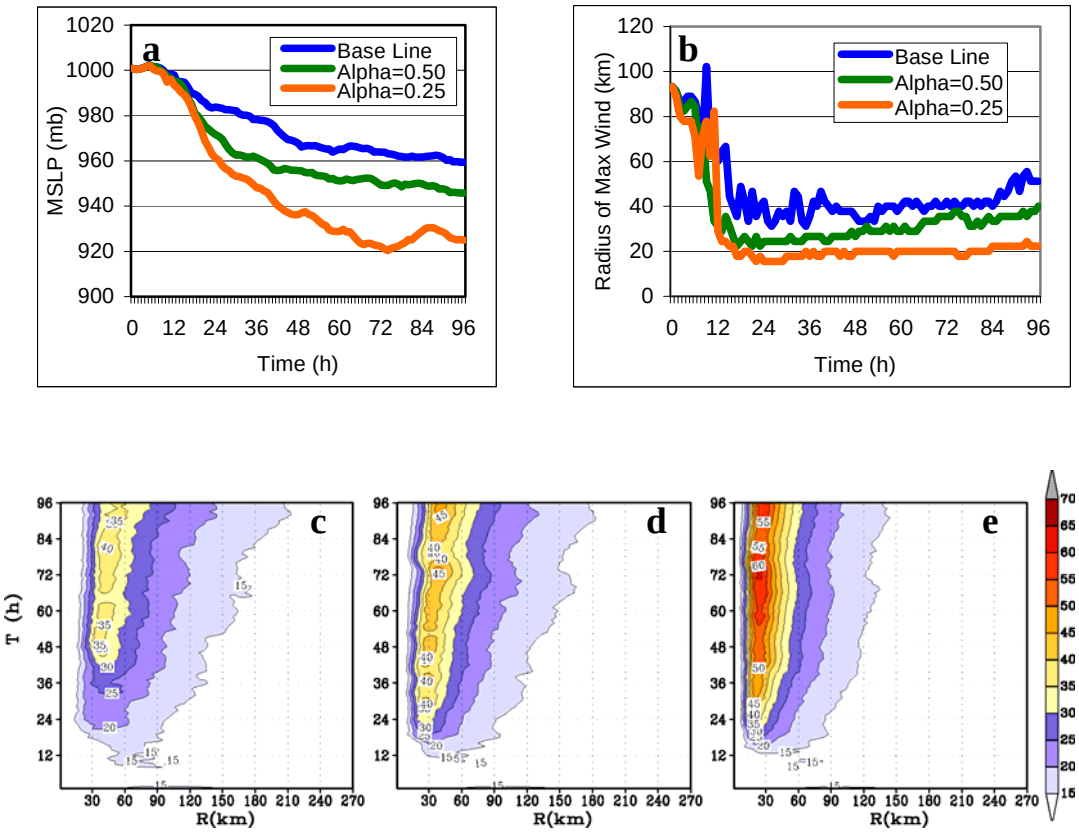

Fig 2. Time history of the intensification process in an idealized storm for the three simulations provided in Table 1: (a) minimum mean sea level pressure in hPa, (b) radius of maximum wind at the first model level; Hovemoller diagram of the axisymmetric mean wind at a height of 10 m for (c) baseline simulation (α=1), (d) Km reduced to half (α=0.50), and (e) Km reduced to a quarter (α=0.25).

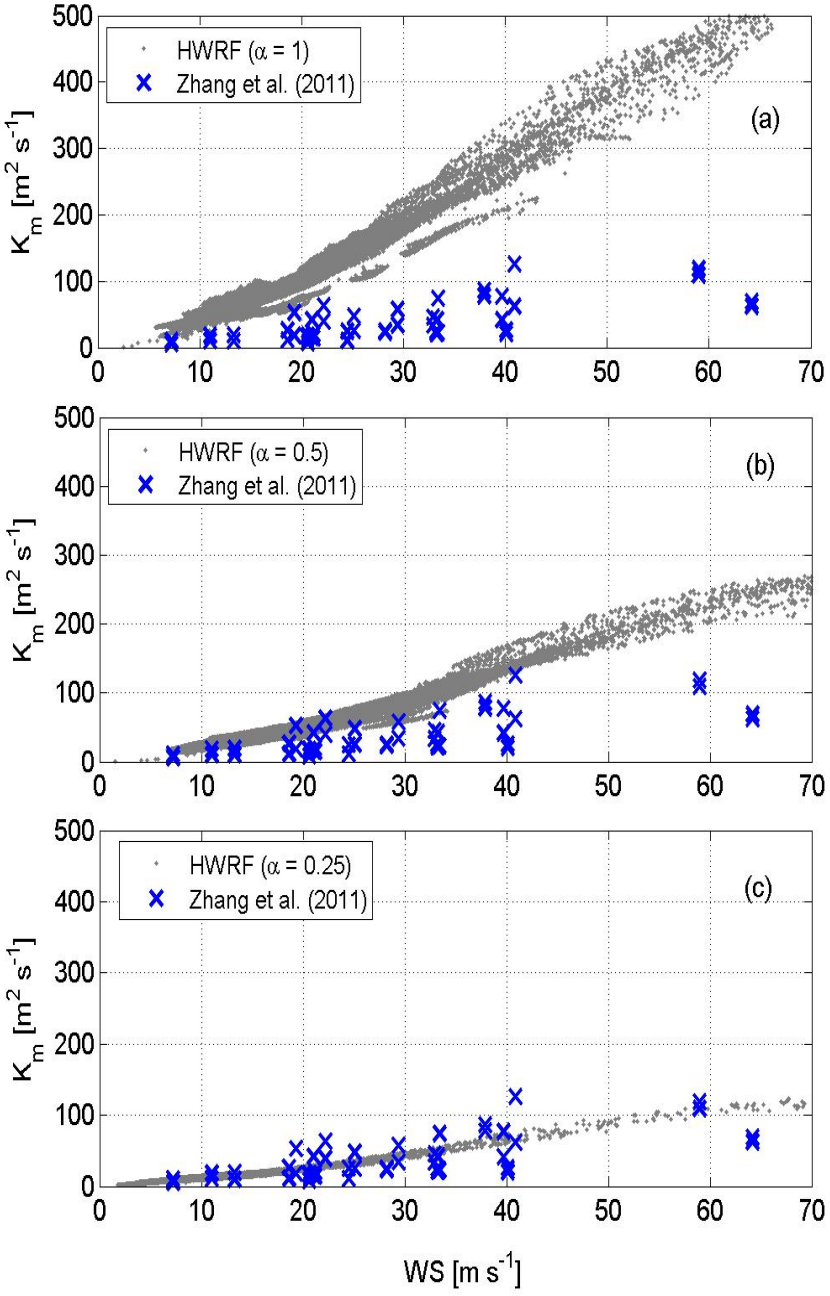

Fig. 3. The variation of the eddy diffusivity coefficient, Km, with 10-m wind speeds; high resolution HWRF model outputs from the (a) control experiment (α=1), (b) Km reduced to half (α=0.50), and (c) Km reduced to a quarter (α=0.25) compared with data from Zhang et al. (2011a) obtained from flight-level data between 450-500 m. Modeled outputs were compared between the same levels.

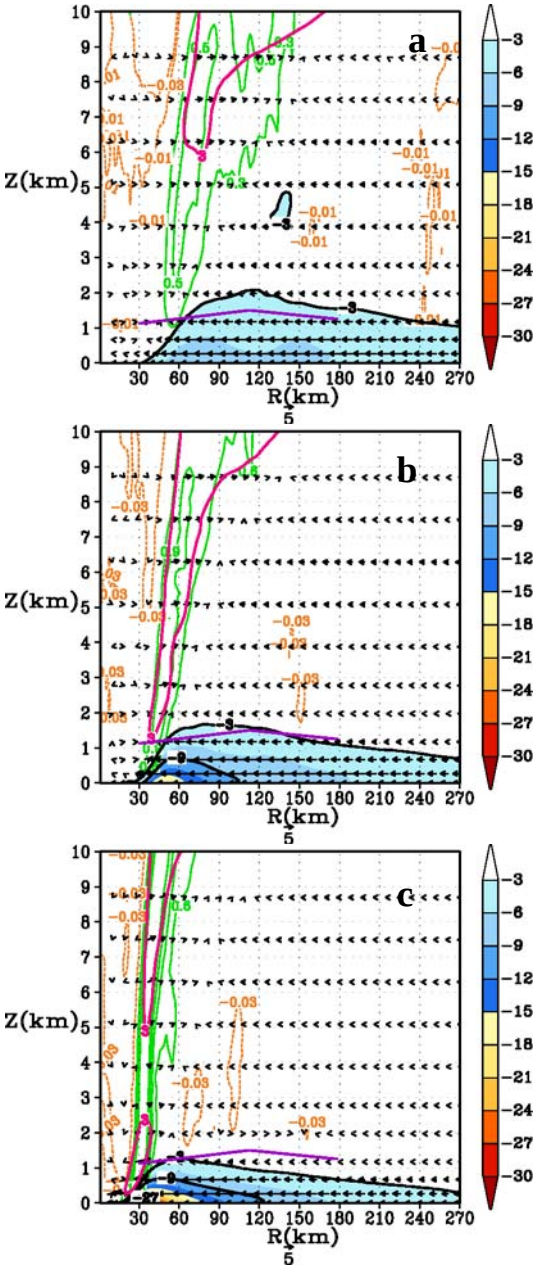

Fig. 4. Tangentially averaged, 6-hourly time averaged, radius-height cross-section of the secondary circulation at 93 hours for (a) control (α=1), (b) Km reduced to half (α=0.50), and (c) Km reduced to a quarter (α=0.25). The black solid contour indicates the inflow, and the magenta contours show the outflow of the radial wind component (in m s^{-1}). Inflow is also shaded in colors. Only the lower 10 km has been expanded for convenience. The vertical velocity (in m s^{-1}) is shown by contour lines with updrafts indicted by green and weak subsidence indicated by yellow. Because the distribution of vertical velocity is skewed, please note that the scales are unequally spaced. For convenience, the vector field obtained that compounded the tangentially averaged vertical and the radial velocity components is also provided here. Presented in purple color are the estimates of the inflow layer depth from Zhang et al. (2011b).

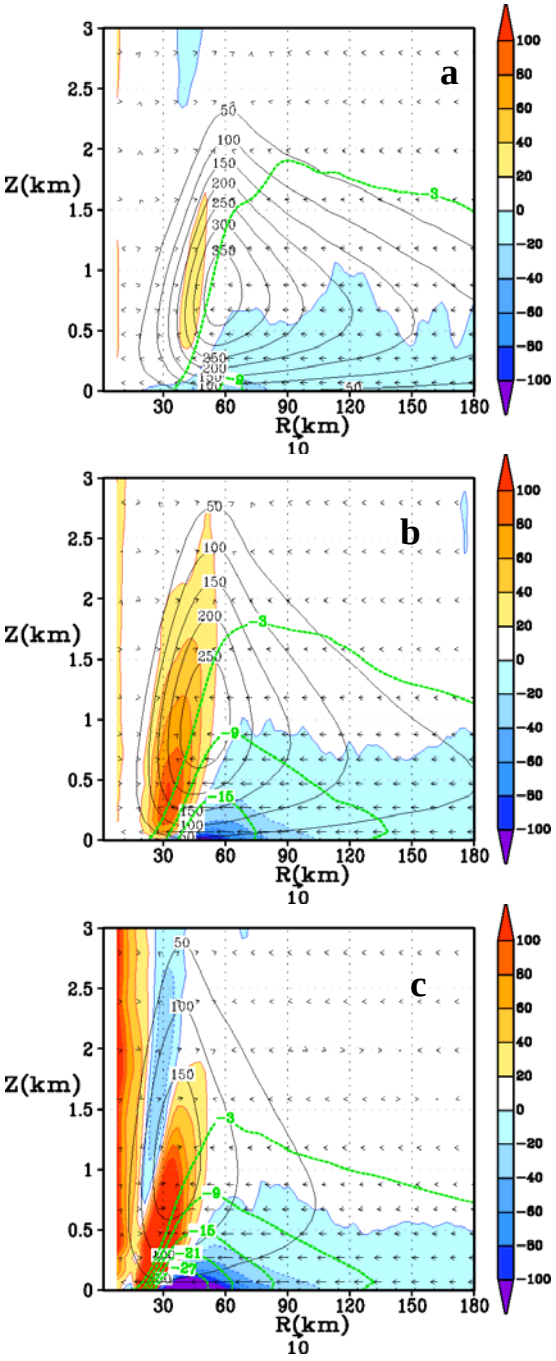

Fig 5: Tangentially averaged, 6-hourly time averaged, radius-height cross section of eddy diffusivity (Km) at 93 hours for (a) control (α=1), (b) Km reduced to half (α=0.50), and (c) Km reduced to a quarter (α=0.25). Superposed in color are the forcing terms related to gradient wind imbalance within the boundary layer (i.e., term B in equation 3). Units of the forcing term are in m s^{-1} h^{-1}. The inflow is shown in the green background contours. For convenience, the vector field that compounded the tangentially averaged vertical and the radial velocity components is also provided. For the sake of clarity, only the first 3 km above the ground is displayed.

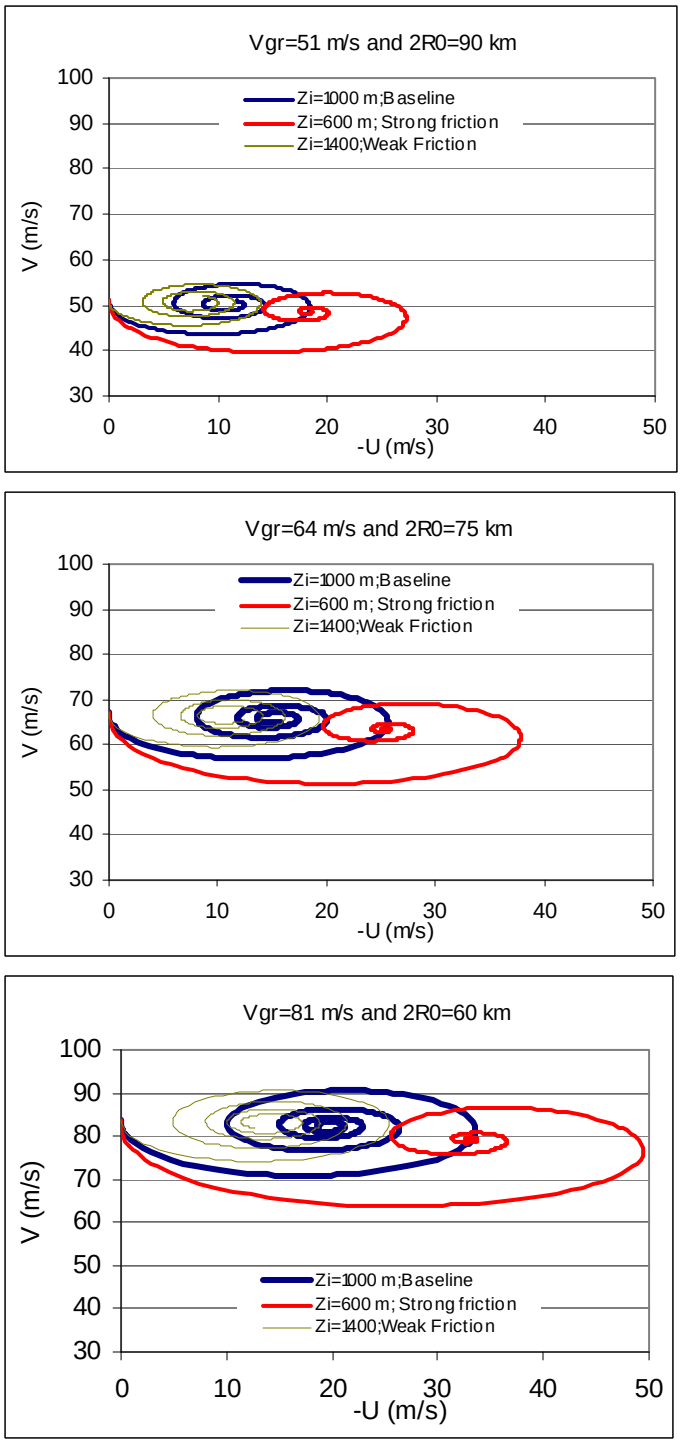

Fig 6: Hodographs obtained for different tangential winds (51, 67, and 84 ms^{-1}) from a simple slab model that was used to provide additional insights on the imbalance of forces within the boundary layer. For each vortex, three boundary layer heights were used, namely, 1000 m (baseline), 600 m (strong frictional force), and 1400 m (weak frictional force).

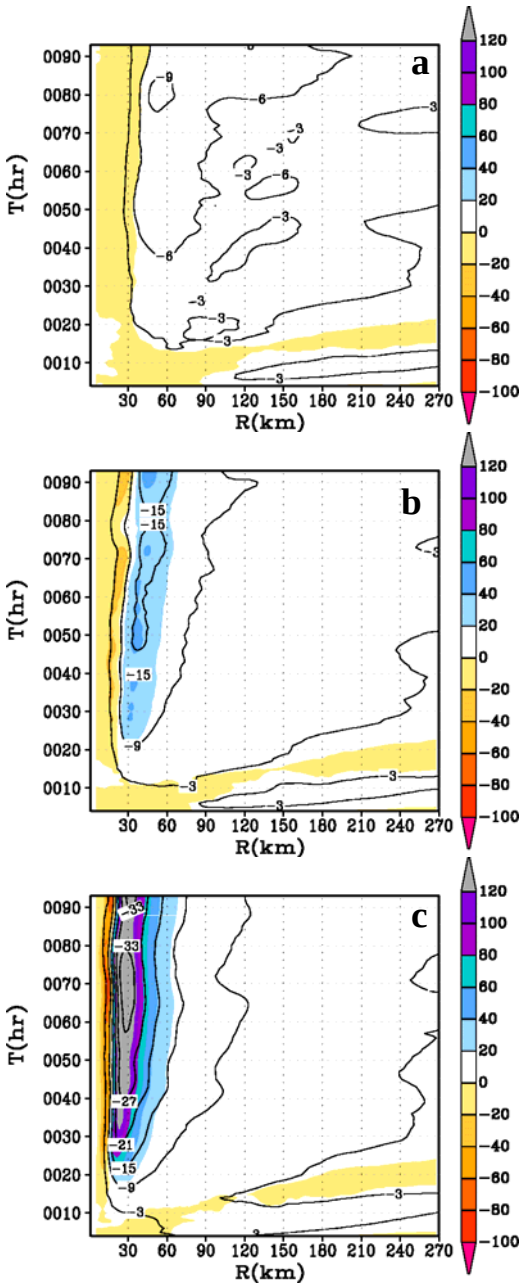

Fig. 7. Hovemoller diagram of the tangentially averaged, 6-hourly time averaged radial component of velocity (in m s^{-1}). Superposed on the contour lines is the generalized Coriolis term (i.e., term A in equation 2 in text) *with the addition of a frictional effect* shaded in color for the HWRF runs with (i) α=1, (ii) α=0.5, and (iii) α=0.25 runs at the 30-m level. The blue end of the spectrum represents tangential acceleration (contributing towards the "spin up"), and the red end of the spectrum represents deceleration within the inner eyewall region. Units of the forcing term are in m s^{-1} h^{-1}.

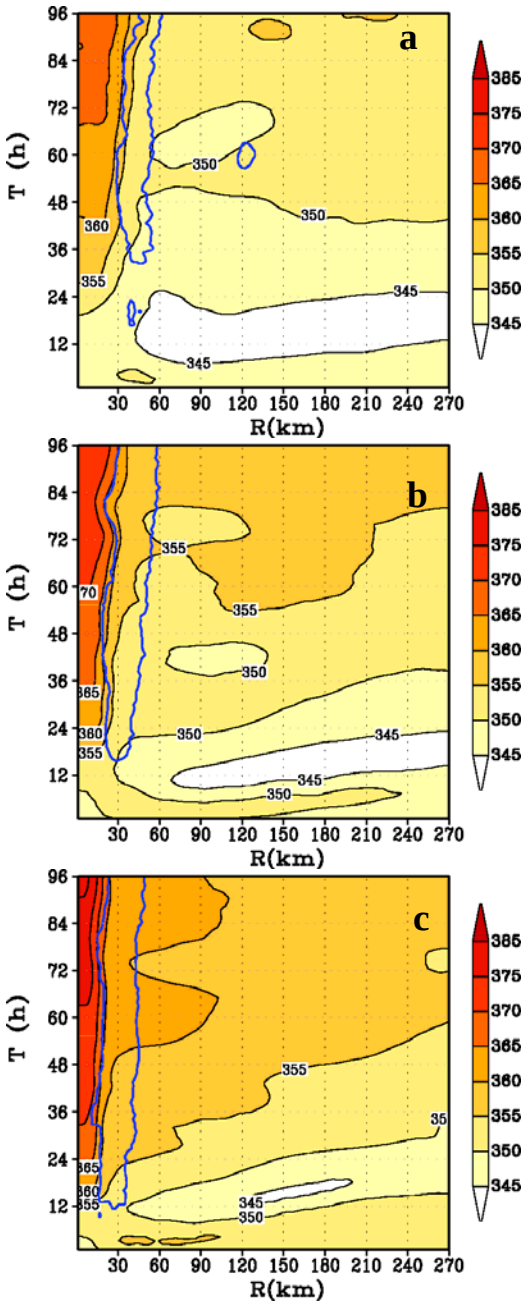

Fig. 8. Hovemoller diagram of the tangentially averaged, 6-hourly time averaged θ_e at the 30-m level for the HWRF runs with (i) α=1 (A100), (ii) α=0.5 (A050), and (iii) α=0.25 (A025). The region of vertical motion exceeding the 0.2 m s^{-1} contour line at the top of the boundary layer is shown to indicate the approximate region of eyewall convection.

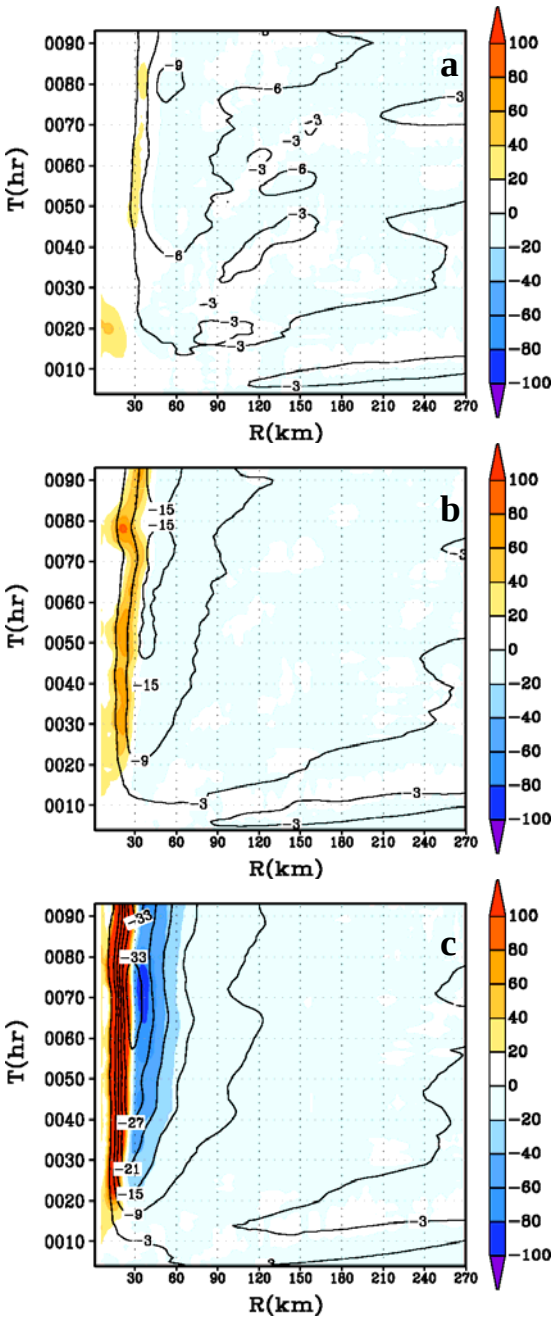

Fig. 9. Hovemoller diagram of the tangentially averaged, 6-hourly time averaged radial component of velocity (in m s^{-1}). Superposed on the contour lines in shaded color is the net radial forcing term *including radial friction* in the governing equation for the secondary circulation (equation 2) for the HWRF runs with (i) α=1, (ii) α=0.5, and (iii) α=0.25 runs at the 30-m level. The blue end of the spectrum represents radial acceleration (convergence), and the red end of the spectrum represents deceleration within the inner eyewall region. Units of the net radial radial forcing term are in m s^{-1} h^{-1}.

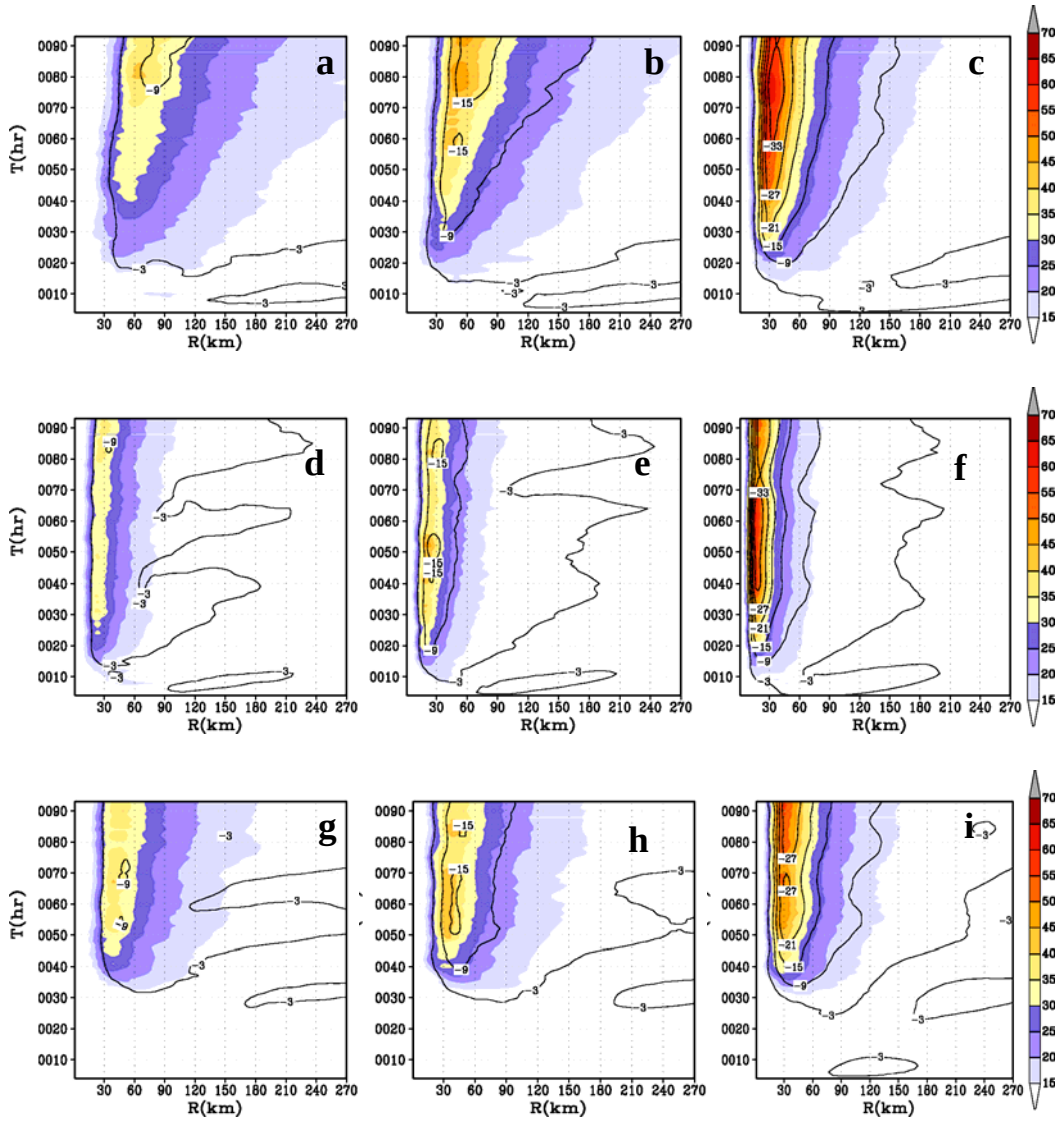

Fig. 10. Hovemoller diagram of the axisymmetric mean winds (m s^{-1}) at a height of 10 m. Contour lines representing the tangentially averaged, 6-hourly time averaged radial component of velocity (in m s^{-1}) at 30-m level are superposed. Top row (a), (b), and (c) are sensitivity experiments for an initially big vortex (experiments 4, 5, and 6 in Table 1). Middle row (d), (e), and (f) are sensitivity experiments for initially small vortex (experiments 7, 8, and 9 in Table 1) and bottom row (g), (h), and (i) are sensitivity experiments in which the relative humidity of the large scale environment was reduced to about 50% from the baseline Jordan sounding. The radius of the initial vortex size for the experiments illustrated in the bottom row (g, h, and i) was set to the base value, i.e., 90 km (Table 1).

Table 1: List of experiments performed

Expt. No	Experiment Names	Description	Initial Radius of Maximum Wind (km)	Relative Humidity	Remarks
1	A100	α=1.00	90	Jordan	Baseline Km & Kh in GFS
2	A050	α=0.50	90	Jordan	Km,Kh reduced to half
3	A025	α=0.25	90	Jordan	Km,Kh reduced to a quarter
4	B100	α=1.00	120	Jordan	Big storm; baseline Km, Kh
5	B050	α=0.50	120	Jordan	Big storm; half Km, Kh
6	B025	α=0.25	120	Jordan	Big storm; quarter Km, Kh
7	S100	α=1.00	60	Jordan	Small storm; baseline Km, Kh
8	S050	α=0.50	60	Jordan	Small storm; half Km, Kh
9	S025	α=0.25	60	Jordan	Small storm; quarter Km, Kh
10	RHA100	α=1.00	90	50% Jordan	Dry storm; baseline Km, Kh
11	RHA050	α=0.50	90	50% Jordan	Dry storm; half Km, Kh
12	RHA025	α=0.25	90	50% Jordan	Dry storm; quarter Km, Kh

Table 2: Simulation statistics gathered during the life time of the storm

Expt. No	Specification	Minimum MSLP (hPa)	Maximum 10-m Wind Speed (ms^{-1})	Maximum Tangential Wind (ms^{-1})	Radius of maximum wind (km)
1	A100	959	47	51	31
2	A050	946	56	64	22
3	A025	925	66	81	16
4	B100	953	49	54	42
5	B050	936	56	66	24
6	B025	910	68	86	22
7	S100	967	45	48	20
8	S050	957	53	60	16
9	S025	930	63	78	11
10	RHA100	964	48	51	33
11	RHA050	957	52	58	27
12	RHA025	932	62	76	22

Table 3: List of experiments performed with a simple slab model

Expt No.	Tangential wind above the slab PBL (ms^{-1})	Depth of slab PBL (m)	Significance of the experiment & analogy with HWRF simulations	Steady state value of radial inflow (ms^{-1})
1	51	1000	Weak vortex baseline (α=1)	12
2	51	600	Weak vortex & strong frictional force	19
3	51	1400	Weak vortex & weak frictional force	9
4	64	1000	Moderate vortex baseline (α=0.5)	16
5	64	600	Moderate vortex & strong frictional force	25
6	64	1400	Moderate vortex & weak frictional force	13
7	81	1000	Strong vortex baseline (α=0.25)	19
8	81	600	Strong vortex & strong frictional force	33
9	81	1400	Strong vortex & weak frictional force	13